Aspect Ratio Determines the Quantity of Mesoporous Silica Nanoparticle Uptake by a Small GTPase-Dependent Macropinocytosis Mechanism

Huan Meng,[†,∥] Sui Yang,[‡,∥] Zongxi Li,[‡] Tian Xia,[†] Justin Chen,[§] Zhaoxia Ji,[⊥] Haiyuan Zhang,[†] Xiang Wang,[†] Sijie Lin,[†] Connie Huang,[§] Z. Hong Zhou,[§,⊥] Jeffrey I. Zink,[‡,⊥] and Andre E. Nel[†,⊥,*]

[†]Division of NanoMedicine, Department of Medicine, [‡]Department of Chemistry & Biochemistry, [§]Department of Microbiology, Immunology, and Molecular Genetics, and [⊥]California NanoSystems Institute, University of California, Los Angeles, California 90095, United States. [∥]These authors contributed equally to this work.

ABSTRACT Although the aspect ratio (AR) of engineered nanomaterials (ENMs) is one of the key physicochemical parameters that could determine biological outcome, not much is understood about how AR contributes to shaping biological outcome. By using a mesoporous silica nanoparticle (MSNP) library that has been constructed to cover a range of different lengths, we could demonstrate that the AR of rod-shaped particles determines the rate and abundance of MSNP uptake by a macropinocytosis process in HeLa and A549 cancer cell lines. MSNPs with an AR of 2.1−2.5 were taken up in larger quantities compared to shorter or longer length rods by a process that is sensitive to amiloride, cytochalasin D, azide, and 4 °C inhibition. The rods with intermediary AR also induced the maximal number of filopodia, actin polymerization, and activation of small GTP-binding proteins (*e.g.*, Rac1, CDC42) that involve assembly of the actin cytoskeleton and filopodia formation. When assessing the role of AR in the delivery of paclitaxel or camptothecin, the rods with AR 2.1−2.5 were clearly more efficient for drug delivery and generation of cytotoxic killing in HeLa cells. All considered, our data suggest an active sensoring mechanism by which HeLa and A549 cells are capable of detecting AR differences in MSNP to the extent that accelerated macropinocytosis can be used to achieve more efficient drug delivery.

KEYWORDS: aspect ratio · macropinocytosis · cell uptake · mesoporous silica nanoparticles · drug delivery · anticancer drug

Due to the rapid evolution in the techniques that are used to synthesize engineered nanomaterials (ENMs), it is possible to construct different shapes from a single base material, including spheres, rods, disks, ellipsoids, and cylinders.[1−5] Besides spherical nanoparticles that have been intensively investigated, nonspherical ENMs with a high aspect ratio (AR) are of great interest since this physicochemical feature has been shown to have a disproportionate impact on biological outcome,[1,3] including determining the rate of cellular uptake,[1] the mechanism of uptake,[1,6] particle transportation,[7,8] biodistribution,[2] and biocompatibility.[9,10] How exactly AR impacts cellular function is unknown, but this information is of considerable importance in understanding how to improve nanomaterial safety and uptake. In order to understand the impact of AR on cellular function, it is necessary to construct an ENM library in which the same base material is used for constructing a range of ARs. One example is synthesis of triacrylate or monomethacrylate nanoparticles through the "particle replication in non-breaking templates" (PRINT) fabrication technique, allowing these investigators to look at the uptake of cylindrical particles that exhibit an AR of 1−3 in HeLa cells.[1] The authors demonstrated that the particles with an AR of 3 (450 nm × 150 nm) were taken up 4 times more rapidly than the particles with an AR of 1. Another example is the use of a set of colloidal gold nanoparticles, composed of spheres (14 and 74 nm) and rods (14 nm × 74 nm) to study cellular uptake in HeLa cells.[4] This demonstrated a 2−4 times higher uptake of spherical gold nanoparticles compared to rod-shaped particles with an AR of 5.

We constructed a mesoporous silica nanoparticle (MSNP) library composed of spherical and rod-shaped particles to study the impact of AR variation on cellular uptake in HeLa and A549 cancer cells. The advantage of using mesoporous silica is that this material is useful for drug delivery as well as studying ENM safety.[11−13] AR effects on MSNP cellular uptake add another design feature that could improve the utility of this multifunctional platform that is being used for drug delivery by controlling pore opening with nanovalves, surface ligation, surface charge variation, *etc.*[12−18] Our data demonstrate that rod-shaped MSNP with an AR of 2.1−2.5 is preferentially endocytosed by an active uptake mechanism that is capable of distinguishing

* Address correspondence to anel@mednet.ucla.edu.

Received for review December 7, 2010 and accepted May 5, 2011.

Published online May 12, 2011
10.1021/nn103344k

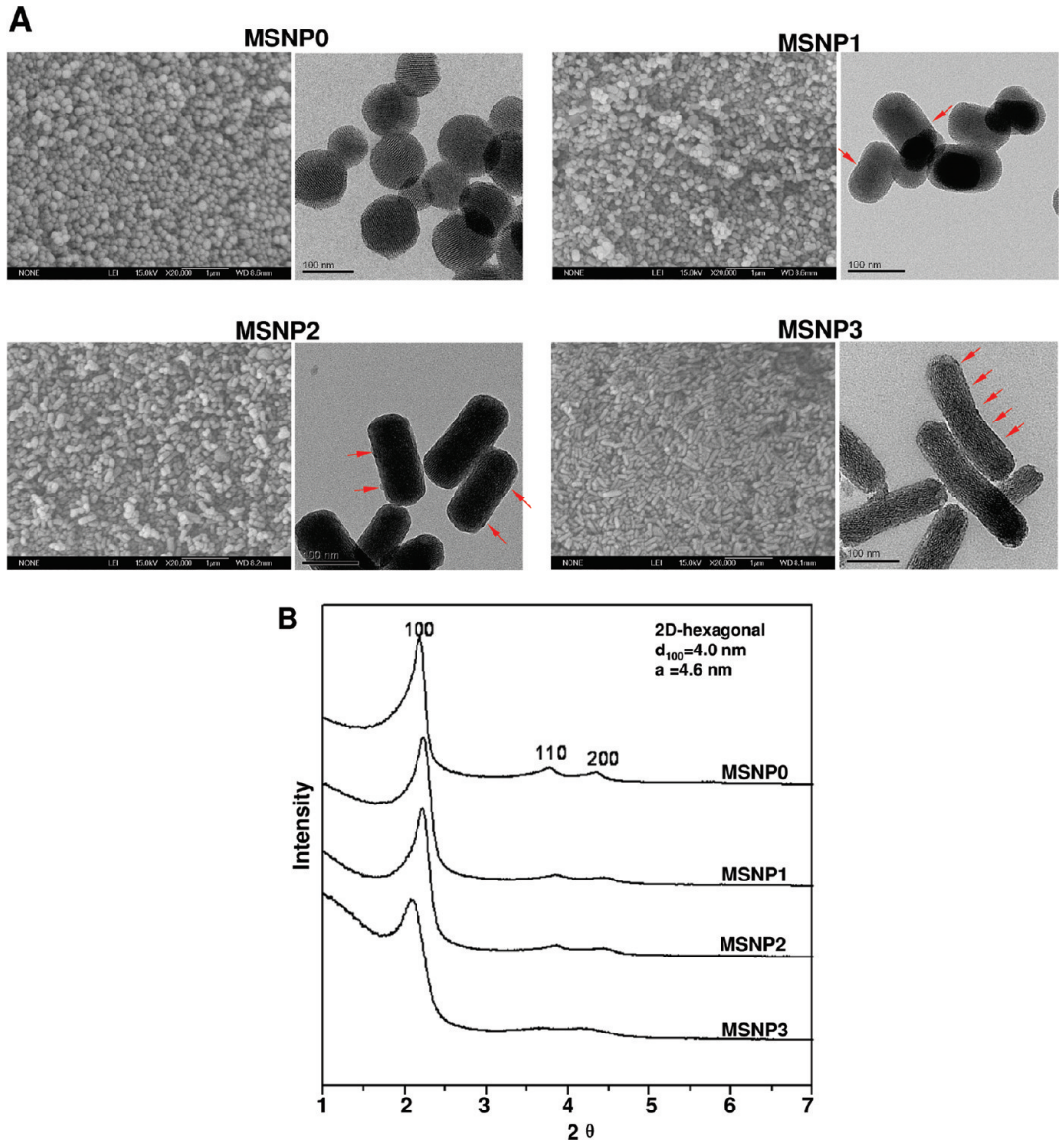

Figure 1. Physicochemical characterization of MSNP. (A) Scanning electron microscope and transmission electron microscope images of MSNP exhibiting different AR values. The arrows point out the periodical "fringes" along the short axes of the rod-shaped particles; these represent ordered helical hexagonal pore arrangements. (B) XRD profiling of MSNP. The peaks confirm the two-dimensional hexagonal symmetry (*p6m*) in the particles. The *d* spacing of the rods was calculated to be 4 nm, using the first diffraction peak and the cell parameter, *a* = 4.6 nm.

intermediary length from longer and shorter rods. This implies a cellular mechanism capable of discerning and responding to rod length. Further investigation of the molecular pathway that involves filopodia formation and macropinocytosis demonstrated intermediary length rods that are capable of small GTPase activation (*e.g.*, Rac1, CDC42), leading to cytoskeletal activation and formation of filopodia. We also observed that the intermediary length rods are more effective for the delivery of chemotherapeutic agents to HeLa cells.

RESULTS

Synthesis and Physicochemical Characterization of MSNPs. MSNPs were synthesized *via* a modified procedure to yield rod-shaped structures.[19] The morphology of the rods, in comparison to the spherical particles, is shown in the SEM and TEM images in Figure 1A. MSNP0 are spheres of ~110 nm diameter, exhibiting uniform pore sizes of 2.5 nm and an AR = 1–1.2 (Figure 1A). By increasing the perfluorooctanoic acid (PFOA)/cetyltrimethylammonium bromide (CTAB) doping ratio during the synthesis, it was possible to obtain rod-shaped cylinders with dimensions of 110–130/60–80 nm (MSNP1), 160–190/60–90 nm (MSNP2), and 260–300/50–70 nm (MSNP3) (Table 1). These values were used to calculate the AR, which varied from 1.5 to 1.7 (MSNP1), 2.1–2.5 (MSNP2), and 4–4.5 (MSNP3). In spite of differences in the AR, the pore structure and pore sizes of the rods are similar (Figure 1 and Table 1). However, with an increase in the AR of the MSNP from 1 to 4.5,

TABLE 1. Physicochemical Characterization of MSNP

samples	MSNP0	MSNP1	MSNP2	MSNP3
aspect ratio	1∼1.2	1.5∼1.7	2.1∼2.5	4.0∼4.5
d_{100} (nm)	4	4	4	4
pore diameter (nm)	2.5	2.5	2.5	2.5
surface area (m^2/g)	1077.9	926.1	896.9	760.2
size in H_2O/RPMI/ CRPMI (nm)[a]	219/1036/239	207/723/229	198/902/337	185/1023/249
zeta-potential in H_2O/CRPMI (mV)	15.7/−5.7	17.1/−6.9	13.0/−5.7	13.5/−6.2

[a] Particle size measurements were performed using dilute suspensions (100 μg/mL) in water or RPMI in a ZetaSizer Nano (Malvern Instruments Ltd., Worcestershire, UK). To disperse the particles, the stock solutions in water (20 mg/mL) were sonicated (Tekmar Sonic Disruptor probe) for 15 s before use. In order to coat the surface of MSNP with FBS, 19 μL of particle suspension was mixed with 1 μL of FBS before addition to complete medium and sonication for 15 s. RPMI denotes the particle size in RPMI cell culture medium without serum; CRPMI reflects the size of MSNP that precoated using FBS in complete RPMI containing 10% FBS.

the surface area of these particles decreased from 1077.9 to 760.2 m^2/g (Table 1). Small-angle powder XRD analysis showed three well-resolved peaks that can be indexed as the 100, 110, and 200 reflections and confirm the hexagonal symmetry (*p6m*) of the pore structure.[20] The rod-shaped particles showed periodical "fringes" along their length (indicated by arrows in Figure 1A), which represent the ordered helical hexagonal pore arrangements as reported in the literature.[19,21,22]

To optimize the particle dispersal for purposes of biological experimentation, the MSNPs were suspended in distilled water containing 5% fetal bovine serum (FBS) and ultimately transferred into complete RPMI containing 10% FBS.[13] Not only does this suspension sequence prevent particle agglomeration due to culture medium ionic effects but it also adjusts the particles' zeta-potentials from positive to negative as a result of protein adsorption (Table 1).

AR Influences Cellular Uptake of MSNPs in HeLa Cells and A549 Cells. Previous publications have shown that a nonspherical shape enhances the abundance and rate of cellular uptake of nanoparticles.[1,3,6,23] In order to assess cellular uptake of FITC-labeled MSNP in HeLa cells and A549 cell line, we used a combination of flow cytometry and confocal microscopy. The fluorescence labeling efficiency is similar for all particle surfaces, allowing us to compare the uptake abundance directly (Figure S1A in Supporting Information S1A). Moreover, comparison of the sedimentation rate during a dynamic assessment of the suspension stability index showed that the spheres and rods behave similarly and do not lead to different rates of settling that could affect cellular uptake (Figure S1B). However, compared to spherical particles (MSNP0), there was a significant increase in the mean fluorescence intensity (MFI) of cells exposed to rod-shaped particles (Figure 2A). This amounted to an 18-, 40-, and 8-fold increase of the MFI for MSNP1, MSNP2, and MSNP3, respectively. Interestingly, the cellular association was consistently higher in MSNP2 than MSNP1 or MSNP3, suggesting that the intermediary AR is preferred for cellular uptake. The preference for a rod *versus* a spherical shape was further confirmed by comparing FITC-labeled spheres and rods with RITC-labeled spheres (Figure 2A). Although there is a slight increase in the uptake of the RITC-labeled spheres in cells that were subsequently treated with FITC-labeled rods, this uptake was small (<3-fold) compared to rods. The small increase likely represents RITC-labeled spheres that are not removed by washing and is internalized during the macropinocytosis of the rods (see below).

The flow data were confirmed by confocal images showing higher uptake of FITC-labeled rods compared to the FITC-labeled spheres (Figure 2B). Moreover, among the rods, the particles with an AR of 2.1−2.5 were endocytosed in greater abundance (Figure 2B) and at a more rapid rate compared to MSNP1 and MSNP3 (Figure 2C). MSNP2 appeared to localize predominantly in the perinuclear region of HeLa cells, whereas MSNP1 and MSNP3 were more randomly distributed (Figure 2B).

To further confirm that the impact of AR is not unique to HeLa cells, the experiments were repeated in the A549 lung cancer cell line (Figure S2 in Supporting Information). Consistent with the HeLa data, MSNP2 yielded the highest cellular uptake compared to spheres or shorter rods in A549 cells (Figure S2).

MSNP2 Uptake Requires Cytoskeletal Activation and Filopodia formation. Electron microscopy (EM) was used for ultrastructural resolution of MSNP uptake in HeLa cells (Figure 3). Although HeLa cells are capable of endocytosing nanoparticles by various routes,[1,24] MSNP2 were taken up by a process of macropinocytosis as evidenced by the presence of filopodia and formation of macropinocytotic vesicles (Figure 3A).[25] Noteworthy, the number of filopodia and extent of membrane ruffling were dramatically enhanced in cells exposed to MSNP2 compared to cells exposed to MSNP3 (Figure 3A) or MSNP1 (not shown). More detailed TEM images of the macropinocytosis process are shown online (Figure S3) together with electron tomography and 3D image reconstruction (Figure S4 and videos 1 and 2). Electron tomography was powerful enough to capture the porous structure of the particles inside the cells, an ultrastructural feature that has not previously been accomplished.

Since macropinocytosis and filopodia formation are dependent on actin assembly at the cell membrane,[26−28] we performed Alexa594 phalloidin staining to visualize these cytoskeletal changes. The confocal images demonstrate that the actin polymerization accompanying filopodia formation is more prominent in cells treated with MSNP2 than the other particle types; this takes on the form of radially distributed spikes that stand away from the ring-like cortical cytoskeleton

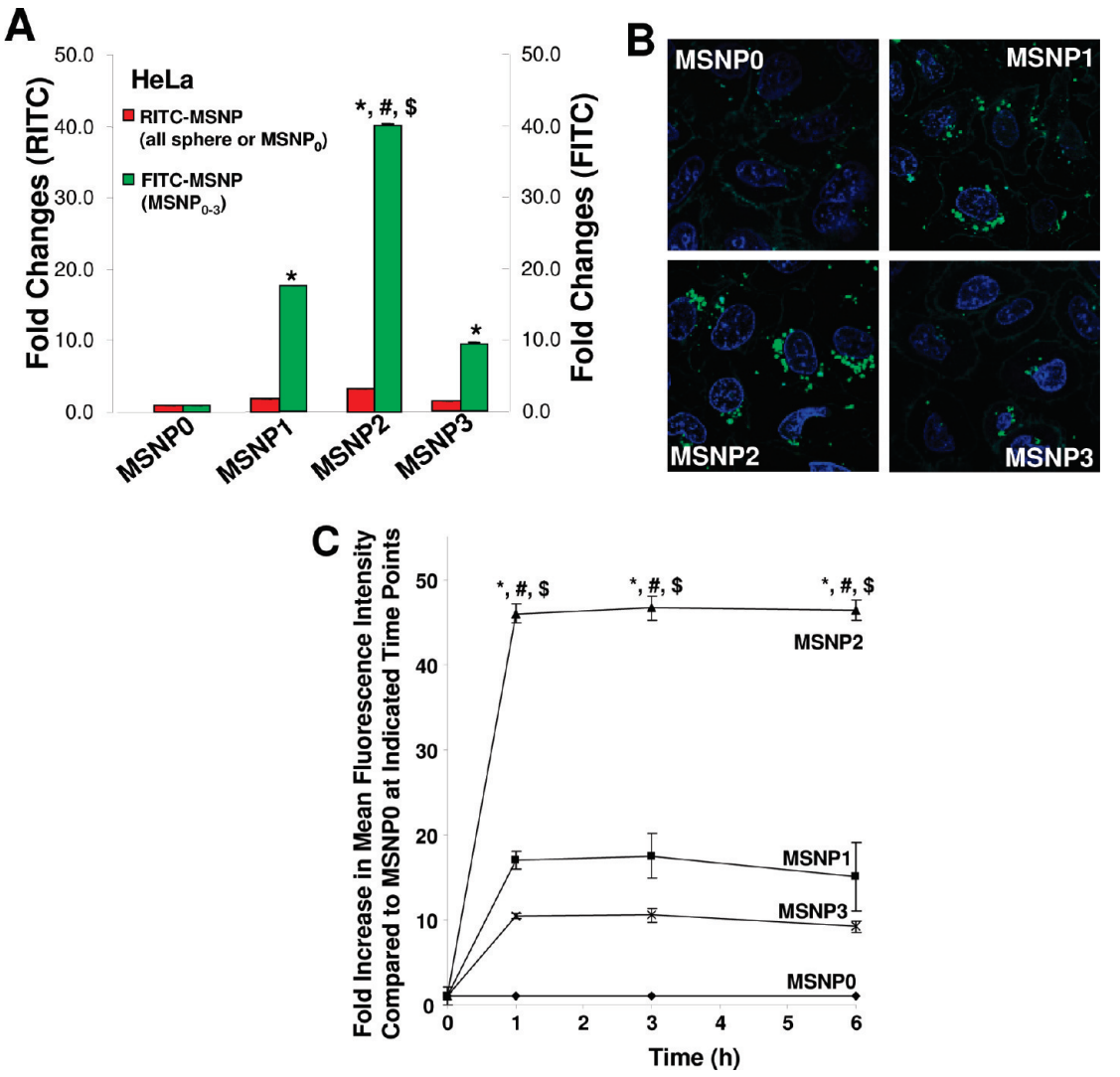

Figure 2. Abundance and rate of cellular uptake of FITC-labeled MSNP in HeLa cells. (A) HeLa cells were treated with 20 μg/mL FITC-labeled particles for 6 h in complete RPMI. The fold increase in mean fluorescence intensity (MFI) compared to spherical FITC-labeled MSNP (MSNP0) was used for comparison. RITC-labeled nanosphere uptake was used as another internal control for comparing each FITC-labeled spheres and rods to an alternatively labeled sphere. The RITC-labeled spheres were introduced 1 h prior to the PBS washing and introduction of the FITC-labeled particles and PBS washing. Prior experimentation has shown that preincubation with RITC-labeled spheres does not interfere in subsequent uptake of FITC-labeled particles. $*$, $p < 0.05$, compared with spherical FITC-labeled MSNP0; #, $p < 0.05$, compared with FITC-labeled MSNP1; \$, $p < 0.05$, compared with FITC-labeled MSNP3. Please note that the small increase in the uptake of the RITC-labeled spheres seen in cells subsequently treated with rods likely reflects a small number of red spheres sticking to the cell surface after washing and then being internalized when the rods activate macropinocytosis. (B) HeLa cells were seeded into 8-well chamber slides before addition of the FITC-labeled particles at 20 μg/mL for 6 h in complete RPMI. After fixation and permeabilization, cells were stained with 5 μg/mL wheat germ agglutinin 633 and Hoechst 33342 dye, followed by visualization under a confocal 1P/FCS inverted microscope. (C) Fold increase in MFI of FITC-labeled rods compared to spheres at 0 to 6 h. HeLa cells were exposed to different FITC-labeled MSNP at 20 μg/mL, and flow cytometry was conducted at the indicated time points. $*$, $p < 0.05$ compared with spherical FITC-labeled particle (MSNP0); #, $p < 0.05$ compared with FITC-labeled MSNP1; \$, $p < 0.05$ compared with FITC-labeled MSNP3.

(Figure 3B, arrow). Scoring of the number of filopodia (spike) by a technique previously published in the literature[29] (and explained in the legend of Figure 3C) demonstrated a 5-, 2.5-, and 1.8-fold increase in filopodia number in cells treated with MSNP2 compared to MSNP0, MSNP1, and MSNP3, respectively (Figure 3C). In addition, the actin assembly in response to MSNP2 was sustained for at least 6 h compared to the transient effects seen with stimuli such as epidermal growth factor.[26]

Chemical inhibitors are widely used to confirm the occurrence of macropinocytosis and as a means of distinguishing this uptake mechanism from clathrin- and caveolae-mediated uptake.[26,30] Prior cellular treatment with amiloride[26] as well as the cytoskeletal inhibitor cytochalasin D (Cyto D)[1,31] decreased MSNP2 uptake by >50% (Figure 3E). These agents also interfered in MSNP2-induced filopodia formation (Figure 3D). Moreover, during the use of filipin to inhibit

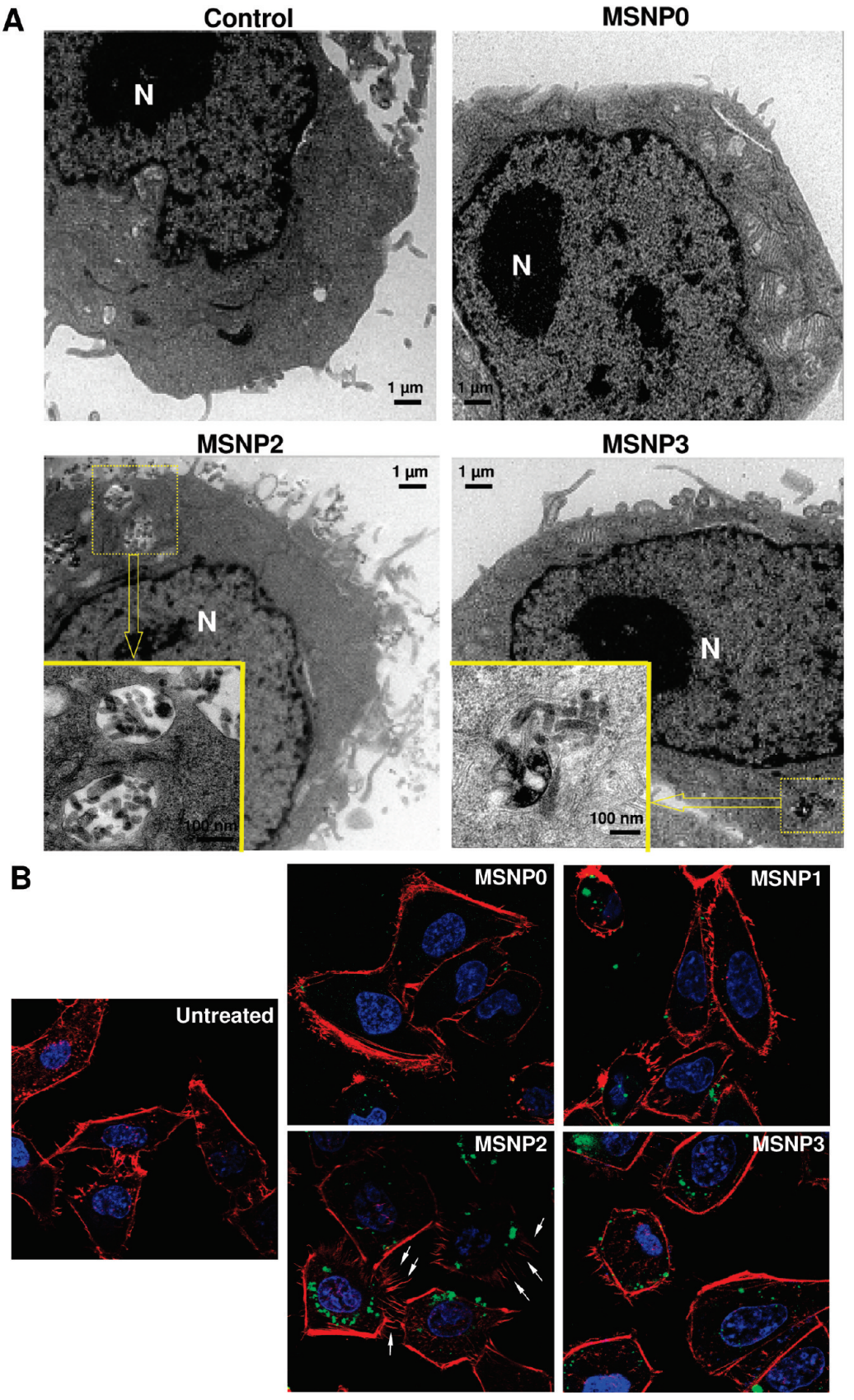
A
Control
MSNP0
N
N
1 μm
1 μm
MSNP2
MSNP3
1 μm
1 μm
N
N
100 nm
100 nm
B
Untreated
MSNP0
MSNP1
MSNP2
MSNP3

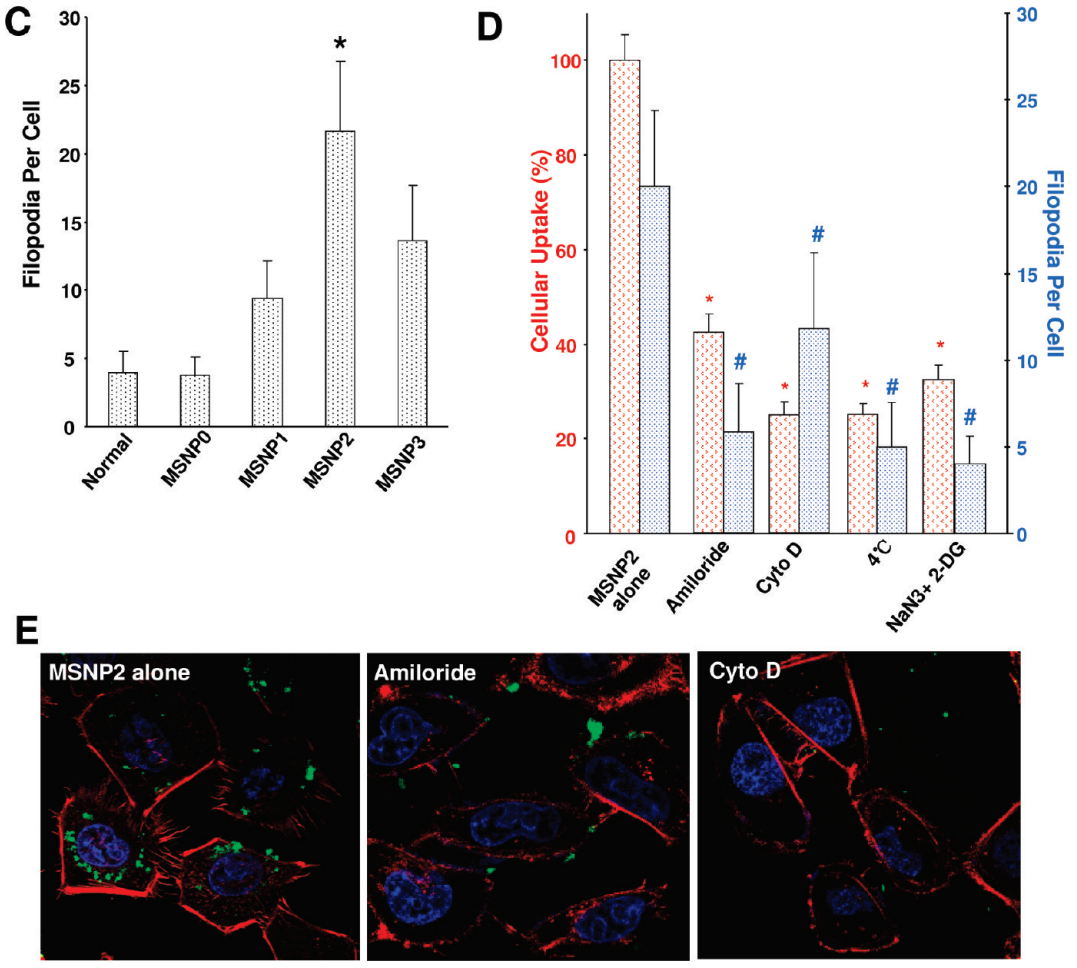

Figure 3. TEM ultrastructural analysis and confocal microscopy to elucidate the role of MSNP uptake by macropinocytosis in HeLa cells. (A) Electron microscopy to determine the ultrastructural changes in HeLa cells following exposure to 20 μg/mL MSNP for 3 h. Notice the increased pinocytotic activity in cells treated with MSNP2 compared to larger or shorter rod-shaped particles. Not only was exposure to MSNP2 accompanied by more prominent membrane ruffles and filopodia formation, but these particles were also taken up more abundant than MSNP1 and MSNP3. "N" denotes nuclear. Additional TEM images are displayed in Figure S3, while a 3D reconstruction using electron tomography is shown in Figure S4 and movies 1 and 2. (B) Confocal microscopy showing the rearrangement of actin fibers as determined by phalloidin staining. Cells were treated with 20 μg/mL spheres or rods for 6 h, fixed, permeabilized, and then stained with Alexa594-labeled phalloidin. Confocal microscopy was performed as in Figure 2. The radial-distributed actin spikes contributing to filopodia formation are indicated by arrows. (C) Quantitative image analysis to determine the number of filopodia per cell. At least 20 cells for each exposure in (B) were used to count the number of actin spikes that comprise the filopodium core; $*$ denotes a significant increase ($p < 0.05$) in cells treated with MSNP2 compared with other particle types. (D) Quantitative expression of the effect of above inhibitors as well as 4 °C on particle uptake and filopodia formation. Significant increase in cellular uptake of MSNP2 and the number of filopodia under various inhibitory conditions compared to treatments using MSNP2 alone. Cellular uptake, $*$, $p < 0.05$, compared to control; number of filopodia, #, $p < 0.05$, compared to control. (E) Confocal microscopy showing inhibition of filopodia formation and FITC-labeled MSNP2 uptake in the presence of amiloride (which is capable of inhibiting Na^+/H^+ exchange) or cytochalasin D (Cyto D) (which is capable of binding to actin filaments and inhibiting actin polymerization).

caveolar uptake through cholesterol sequestration[32] as well as employing monodansylcadaverine to inhibit formation of clathrin-coated pits,[33] we did not observe any interference in MSNP2 uptake in HeLa cells (Figure S5A). The energy dependence of the macropinocytosis pathway was confirmed by culturing the cells at 4 °C[34] or pretreating them with sodium azide (NaN_3)/2-deoxyglucose (2-DG) for 3 h before the addition of the particles (Figure S5B).[1] The latter inhibitors also decreased filopodia formation and MSNP uptake by >60% (Figure 3D).

To study the subcellular fate of endocytosed MSNP2, confocal microscopy was used to localize FITC-labeled MSNP2 in relation to clathrin-coated vesicles, caveolae, and lysosomes in HeLa cells (Figure S6).[35] These endocytotic compartments were localized by RITC-labeled secondary antibodies capable of binding to primary antibodies recognizing clathrin, caveolin-1, and LAMP-1, respectively. ImageJ software analysis to quantify FITC-labeled MSNP2 colocalization with labeled compartments showed that, while <1% of these rods were localized in clathrin or caveolin-1 stained compartments (Figure S6, upper panel), more MSNP2 entered a LAMP-1 positive compartment (Figure S6, lower panel). Thus, while <5% of the

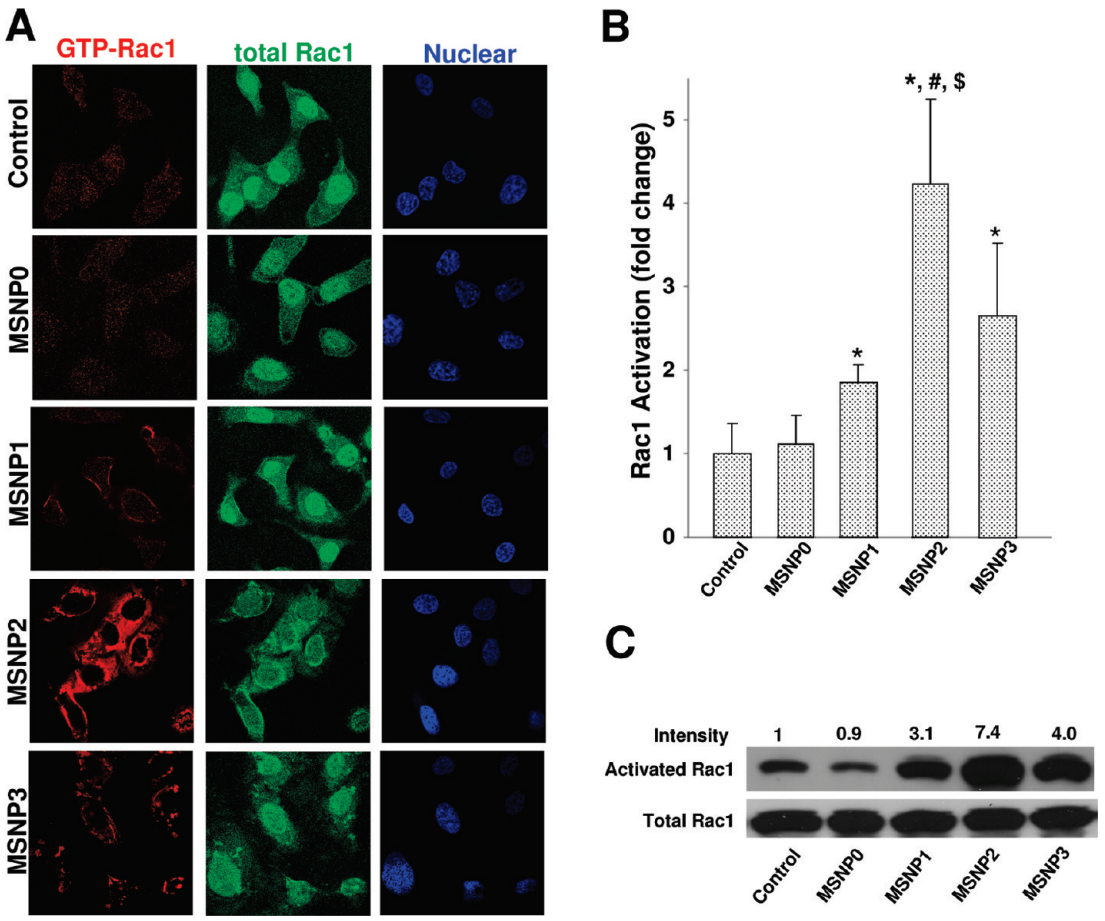

Figure 4. Confocal microscopy and pull-down assay to show the effect of the different particle types on Rac1 activation in HeLa cells. (A) Cells were serum-starved for 4 h before the introduction of the particles, which were dispersed in complete RPMI. In order to correct for effect of serum growth factors on Rac1 activity, we also included serum-starved control that was treated with complete RPMI for 30 min. Particles were introduced at 20 μg/mL in complete RPMI for 30 min. After fixation and permeabilization, cells were stained with primary antibodies recognizing GTP-Rac1 or total Rac1, which were subsequently visualized with Alexa594 or FITC-labeled secondary antibodies, respectively. Nuclei were stained with Hoechst dye. (B) Fluorescence intensity of GTP-Rac1 in (A) was quantitatively analyzed using ImageJ software. The fluorescence intensity of serum-starved control cells exposed to complete medium for 30 min (A, first row) was used as the reference value for calculating the particle-induced increase in Rac1 activation. At least 20 cells from the selection shown in panel A were used to perform the analysis. $*$ denotes a significant decrease ($p < 0.05$) for each particle type with the control. #, $p < 0.05$, compared with MSNP1; $, $p < 0.05$, compared with MSNP3. (C) Rac1 activation was further confirmed by a pull-down assay using that Rac activation assay kit from NewEast Biosciences (Malvern, PA). After similar particle treatments as in (A), HeLa cells were instantly lysed in ice-cold lysis buffer and anti-GTP-bound Rac1 monoclonal antibody was added to the cell lysates. The bound, active Rac1 protein was then captured by protein A/G agarose and subsequently detected by Western blotting using a second anti-Rac1 antibody. The total Rac1 protein was detected by Western blotting using anti-Rac1 antibody (Santa Cruz Biotechnology, CA).

particles entered the LAMP-1 positive compartment by 6 h, this fraction increased to 75% by 36 h. All considered, these data indicate that MSNP2 are primarily taken up by macropinocytosis and are ultimately transferred to an acidifying endosomal compartment that specializes in particle degradation. Interestingly, the MSNP-laden lysosomes could be seen to change their localization from a random to a clustered arrangement in the cell (Figure S6, bottom right panel). The significance of this redistribution is uncertain.

MSNP2 Promotes Active Macropinocytosis through the Activation of Small GTPases. Macropinocytosis is frequently triggered by external stimuli, such as viruses[25] or growth factors[36] capable of activating membrane-associated signaling cascades that play a role in actin polymerization and plasma membrane ruffling.[26,30] One of the signaling mechanisms involves the activation of the GTP-binding protein, Rac1, which plays a role in membrane ruffling, cytoskeletal changes, and closure of the macropinosome.[26,30] In order to see if Rac1 is activated during MSNP macropinocytosis, we used an immunochemical technique that distinguishes activated GTP-bound Rac1 from total cellular Rac1 protein.[37−39] This was accomplished by using a secondary Alexa594-conjugated antibody that recognizes anti-GTP-Rac1 as well as a FITC-labeled secondary antibody that binds to anti-Rac1 capable of recognition of frame site in Rac1.[37−39] Use of these antibody

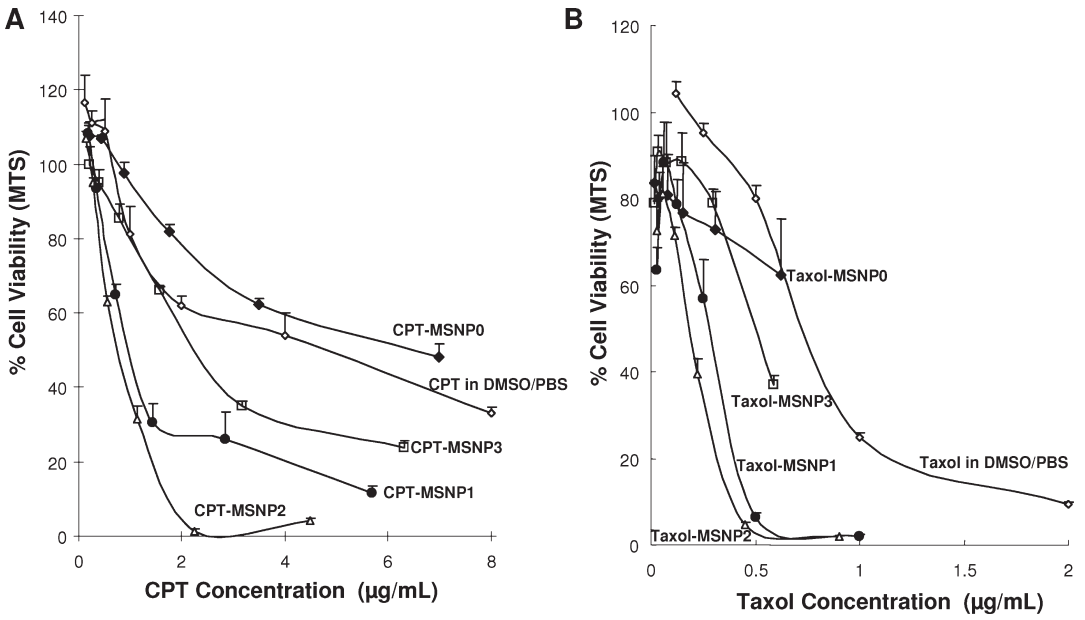

Figure 5. MTS assay comparing the cytotoxic effects of free CPT and Taxol delivered by the different MSNP types. (A) Comparison of the CPT effects in HeLa cells. After incubation with the particles for 36 h at doses of 6.25−200 μg/mL (which agrees with CPT concentrations of 0.1−8.0 μg/mL), the cells were incubated with the MTS reagent for 2 h and the absorbance measured at 490 nm. (B) Same experiment was performed using Taxol. The cells were treated for 36 h at particle concentration at 6.25−200 μg/mL, which equals Taxol concentrations of 0.1−2.0 μg/mL for 36 h. The MTS assay was performed as in panel A.

combinations for confocal studies in HeLa cells showed more intense Rac1 activation (red fluorescence) in cells treated with MSNP2 compared to cells exposed to MSNP0, MSNP1, or MSNP3 (Figure 4A). In contrast, the total Rac1 abundance (green fluorescence) remained the same across the cell populations. Use of ImageJ software to calculate the increase in Alexa594 fluorescence demonstrated a significant increase in abundance of activated Rac1 following MSNP2 treatment (Figure 4B). Longer and shorter rods induced less prominent Rac1 activation (Figure 4B). These response differences were sustained for at least 30 min. Rac1 activation by the rod-shaped particles was further confirmed by a pull-down assay, which demonstrated that while the total amount of Rac1 as determined by immunoblotting was stably expressed, there was an approximate 7-fold increase in the abundance of activated Rac1 in response to MSNP2 treatment compared to the control (Figure 4C). This is in accordance with the confocal data showing an approximate 2-fold increase for MSNP2 compared to MSNP1 or MSNP3-treated cells. Noteworthy, Rac1 activation was suppressed in MSNP2-exposed cells treated with amiloride, NaN_3/2-DG, or cultured at 4 °C (Figure S7 in Supporting Information). In contrast, Cyto D, which functions downstream of Rac1, had no significant effect (Figure S7). To further validate the role of Rac1 in MSNP2 uptake, we also looked at the effect of Rac1 knockdown by transfection of a small interfering RNA (siRNA) that targets at Rac1 protein. A nonrelevant siRNA targeting GFP protein was used as control. While the Rac1 siRNA achieved ~75% protein knockdown efficacy (Figure S8, immunoblot insert) and reduced MSNP2 uptake (as determined by flow cytometry) by ~90%, the nonrelevant siRNA had no knockdown effect but still reduced MSNP2 uptake by ~60% (Figure S8). This is likely due to the cytotoxicity of the transgenic agent, Lipofectamine 2000,[40] or could be due to a possible "off-target" effect of siRNA treatment resulting in global effects on protein expression in cells.[41] However, Rac1 siRNA did exert a statistically significant effect on cellular uptake compared to the nonrelevant siRNA treatment.

In order to complement the Rac1 data, activation of other small GTPases that may act in concert with Rac proteins during endocytosis was considered. These include CDC42, a member of the Rho subfamily that controls diverse cellular functions, including regulation of macropinocytosis by actin polymerization in an amiloride-sensitive pathway.[42] Utilizing a G-LISA activation kit (Cytoskeleton, Inc.), we demonstrated more CDC42 activation in cells treated with MSNP2 compared to cells exposed to spherical or other rod-shaped particles (Figure S9). Another small GTPase is RhoA, which regulates the actin cytoskeleton during the formation of stress fibers and may be transiently activated during macropinocytosis.[43] However, through the use of the G-LISA activation kit, we could not discern any RhoA activation by MSNP treatment (not shown).

Delivery of Hydrophobic Chemotherapeutic Agents by Long AR Particles. Due to the ordered porous structure and large surface area capable of cargo loading, MSNPs have emerged as a multifunctional drug delivery platform.[11−15,44] In light of the facilitated cellular

uptake of MSNP2, we compared the cytotoxic effects of two hydrophobic chemotherapeutic agents, camptothecin (CPT) and paclitaxel (Taxol), delivered by spherical and long AR particles. The drugs were loaded into the particles by soaking them into the pores through the use of an organic solvent and then performing phase exchange by washing the particles in an aqueous buffer as previously described by us.[11−13] The efficacy of the different particle types in cellular killing was assessed by a MTS assay. Use of this assay to compare equivalent amount of drug being delivered over a 36 h time period demonstrated that the cytotoxic potential of drug-laden MSNP2 > MSNP1 > MSNP3 > MSNP0 (Figure 5). The particles themselves were devoid of any toxicity, as shown in Figure S10.

DISCUSSION

In this paper, we demonstrate that HeLa and A549 cells endocytose rod-shaped MSNPs through a macropinocytosis process that is capable of discerning the AR and adapting the cellular response so that uptake is maximal for particles with an AR of 2.1−2.5. This differential effect involves filopodia formation that is linked to activation of the actin cytoskeleton by a small GTP-binding protein. These findings suggest a mechanosensitive process that is capable of translating variations in AR into small GTPase activation, including Rac1 and CDC42. Particles taken up into the pinocytotic vesicles are shuttled into an acidifying lysosomal compartment and can be used to deliver hydrophobic chemotherapeutic agents. This utility was demonstrated by the delivery of Taxol and CPT in HeLa cells, with optimal cytotoxicity being achieved when the drugs are loaded into rods with an AR of 2.1−2.5.

Current research in the field of biomaterials is witnessing the emergence of a powerful set of new design parameters, including the use of physical shape at micrometer and nanoscale levels to control biological responses.[3,8,10,45,46] Shape is an important physical characteristic and has an important role in modeling cellular responsiveness and associated applications in biotechnology.[1] Theoretical models and experimental studies have confirmed the benefits of using nonspherical particles for drug delivery based on their effects on cellular internalization and vascular dynamics.[1,2,7,47] This includes the observation that for micrometer-size particles the local geometry at the point of contact with the cell membrane rather than the overall particle shape dictates whether macrophages initiate internalization.[45] In this regard, it has been demonstrated that when a macrophage encounters an elliptical disk at its pointed edge or side, the particle is rapidly phagocytosed within minutes, whereas attachment to the flat side of the disk failed to initiate phagocytosis for an extensive time period.[6,8,45,48] The effect of geometry in phagocytosis could be quantified by measuring the angle between the membrane at the point of initial contact and the line defining the particle curvature at this point. If this angle exceeds a critical value of >45°, the cells lost the ability to entrap the particles.[3,45] The authors proposed that the particle shape at the point of attachment determines the type of actin rearrangements that are required for cellular uptake.[3,45] According to this view, the requisite actin structures cannot form if the angle is >45°, leading the macrophages to switch to an alternative spreading behavior.[45]

At a much smaller length scale, Gratton *et al.* demonstrated that internalization of cylindrical particles depends on AR.[1] In this elegant study, the authors evaluated internalization pathways of three different series of micro- and nanosized particles made from the cross-linked PEG-based hydrogels produced by the PRINT technique.[1] The synthesized materials included cubic microparticles, cylindrical microparticles, and cylindrical nanoparticles (200 × 200 nm; 100 × 300 nm; 150 × 450 nm). While all of the particles were internalized by HeLa cells, the nanoparticles entered more rapidly, with the longer cylinders (150 × 450 nm) being captured more rapidly than cubic particles of nearly similar volume (200 × 200 nm) or shorter cylinders of lower volume (100 × 300 nm). Particles with an AR of 3 were internalized about 4 times more rapidly than spheres of the same volume.[1] In contrast to the results for hydrogel particles, other studies have found that receptor-mediated endocytosis of Au nanoobjects was significantly decreased with increased AR.[4,49,50] For instance, Au nanospheres with diameters of 14 or 74 nm were endocytosed 3 times more readily by HeLa cells compared to 74 × 14 nm rods.[4] Muro *et al.* compared targeted accumulation of spheres of various diameters (ranging from 100 nm to 10 μm) or elliptical discs of microscale dimensions (1 × 3 μm) in tissues and found that the targeting efficiency of micrometer-scale discs is better than spheres, even those with nanoscale dimensions.[51]

This paper enhances our understanding of the role of AR by demonstrating that for MSNP of the same chemical composition there is differential macropinocytosis of particles with an AR 2.1−2.5. Moreover, this effect is mediated through a pathway that involves the activation of small GTP-binding proteins (*e.g.*, Rac1), the actin cytoskeleton, and filopodia formation.[52] Not only is the demonstration that Rac1 and CDC42 activation by rod-shaped MSNP a novel finding but it also provides a platform for understanding how specific shape variations can be used to modulate cellular function. Macropinocytosis refers to the formation of large endocytic vesicles of irregular shape and size that is generated by actin-driven evaginations of the plasma membrane.[26] Macropinocytosis is an efficient route for the nonselective uptake of soluble macromolecules and is either constitutive or stimulated by growth factors such as epidermal growth factor, platelet-derived

growth factor, macrophage colony-stimulating factor, interleukin-4, or phorbol esters.[26,30,53] It has been reported that antibody conjugates directed against intercellular adhesion molecule (ICAM-1) or platelet–endothelial cell adhesion molecule (PECAM-1) can promote drug delivery by vehicles that are recognized and internalized by endothelial cells through macropinocytosis.[54] Interestingly, these agents are all capable of initiating signaling pathways that activate small GTPases, which have also been shown to play a role in regulating macropinocytosis.[36] The occurrence of macropinocytosis in a variety of different cell types suggests that it contributes to cellular functions such as nutrient uptake,[55] host–pathogen interactions,[56] antigen processing,[57] and directed cell movement.[55] Macropinocytosis differs from other endocytic mechanisms that are involved in the uptake of individual nanoparticles by smaller vesicles.[26] Different from clathrin-dependent, caveolae-mediated, or caveolae- and clathrin-independent pathways,[58] macropinocytosis is dependent on signaling to the actin cytoskeleton and actin-driven membrane movement.[26,35] This results in membrane ruffling and the formation of filopodia that are necessary for the closure of the macropinocytotic vesicles.[26] The intracellular fate of macropinosomes varies depending on the cell type but in most cases ends up fusing with lysosomes and shrinking.[55]

A key question that remains is how the differences in AR are being discerned and translated into small GTPase activation and actin assembly in HeLa and A549 cells. While we do not have an exact explanation, it is worthwhile to consider the role of the integrated adhesome network that responds to complex chemosensitive and mechanosensitive environmental cues in the extracellular matrix (ECM).[59] Cells demonstrate an extraordinary ability to respond to a wide range of physical signals, either locally or globally, and are capable of reacting to ECM topography, including its rigidity,[60] spatial organization, and anisotropy.[59,61] The crucial scaffolding interactions involved in the link of the ECM to the actin cytoskeleton involve actin-polymerizing and actin-linking modules associated with the integrin–receptor system.[59] This system as a whole is mechanoresponsive, and numerous studies have demonstrated that the biochemical characteristics of the ECM, including its spatial organization, are recognized by cells as a result of differential signaling from integrin-based molecular complexes.[59,62] This molecular machinery can be viewed as a network of tightly interconnected modules that contains ~700 links, most involving binding interactions with the rest consisting of pathways that modify those interactions.[59] The biological activities of the adhesome components are quite diverse and include several actin regulators that affect the organization of the attached cytoskeleton. These include adapter proteins that link actin to integrins (directly or indirectly) as well as a wide range of signaling molecules, including kinases, phosphatases, GTP-binding proteins, and their regulators.[59]

How could this model apply to the sensing and response to AR variations of a nanomaterial? While it is unlikely that integrins are directly involved in this process, MSNPs may be decorated with serum proteins that could act as ligands on the particle surface. However, we regard this as an unlikely explanation because macropinocytosis differs from receptor-mediated endocytosis that classically proceeds *via* caveolae or clathrin-mediated uptake. Another possibility is that AR variation could be detected at the contact site of the nanoscale spheres and rods with the cell surface membrane or the lipid bilayer lining the macropinocytotic vesicles. In this regard, it has been demonstrated that silanol groups on silica nanoparticles are capable of interacting with membrane lipid compounds and possibly also with electrostatically charged membrane proteins.[63,64] It is possible that the number and spatial distribution of these contact sites may be capable of relaying information to small GTPases by a transduction process that either involves GTP loading *via* a guanine nucleotide exchange factor or inhibiting the activity of the GTPase. The exquisite sensitivity of cells to variations in adhesive patch spacing at the nanoscale level has been demonstrated through the use of nanolithography approaches, for example, positioning of nanoscale gold particles (1–15 nm) in spatial arrangements or formation of spacing gradients that can be tuned at 10–200 nm scales.[59,65,66] Examination of cellular spreading on these surfaces has demonstrated that the weakest gradient to which cells can respond corresponds to a strength of ~15 nm per mm, provided that the interparticle spacings remained at 58–73 nm.[59,67,68] Given a typical spreading length of 60 μm, the implication is that cells can respond to 1 nm differences in average ligand patch spacing between the front and rear end of the cell.[59] Thus, the sensitivity to small variations in interparticle spacing is quite remarkable and probably achievable in a time-integrated manner.[59] Interestingly, these variations are much smaller than the typical variations in the interligand spacing that governs integrin interactions with the ECM. Thus, given this exquisite sensitivity at the nanoscale level, we propose that a related mechanism may be involved in detecting AR differences in rod-shaped MSNP.

These results not only advance our understanding of the mechanism by which AR differences change cellular uptake but also allow us to add a shape design feature to the list of tunable MSNP properties that can be exploited to improve drug delivery.[11,15,69,70] Accumulated evidence indicates that spherical nanocarriers may not be optimal drug delivery devices due to the poor cellular uptake and unsatisfactory biodistribution compared to disk-shaped objects or particles exhibiting a long AR.[1,2,7] To improve cellular uptake of MSNP, we

have previously shown that better uptake can be achieved by noncovalent attachment of the cationic polymer, polyethyleneimine, to the particle surface.[12,13] However, cationic functionalization could lead to cytotoxicity.[12,13] We now demonstrate improved delivery and killing in HeLa cells by using an optimal AR of 2.1−2.5 (Figure 5). To further understand the biobehavior of AR particles *in vivo*, we are currently performing animal experiments to test the efficacy of a nonspherical MSNP delivery system.

CONCLUSION

We demonstrate through the use of AR variation in a designed MSNP library that cells actively respond to the shape change by changing particle uptake through a macropinocytosis process. Not only can HeLa and A549 cells distinguish between specific ARs, but they are also capable of translating this recognition into activation of small GTPase such as Rac1, control actin assembly, and optimal filopodia formation that leads to maximal uptake of intermediary length rods. This active uptake process can be inhibited by a list of inhibitors (amiloride, Cyto D and NaN_3/2-DG) or dropping the culture temperature to 4 °C. We also demonstrate that intermediary length MSNPs with an AR of 2.1−2.5 are more efficient for delivery hydrophobic chemotherapeutic agents to HeLa cells.

MATERIALS AND METHODS

Experiment Reagents. Commercial reagents and analytical materials used in this study included tetraethoxysilane (TEOS, 98%, Aldrich), cetyltrimethylammonium bromide (CTAB, 98%, Aldrich), perfluorooctanoic acid (PFOA, 96%, Aldrich), methanol (99.9%, Fisher), triethylamine (99.5%, Aldrich), ethanol (200 proof, Pharmaco-AAPER), 3-aminopropyltriethoxysilane (APTES, 99%, Gelest), rhodamine-B-isothiocyanate (RITC, Aldrich), fluorescein isothiocynate (FITC, >90%, Aldrich), amiloride (Aldrich), cytochalasin D (Aldrich), filipin (Aldrich), monodansylcadaverine (Aldrich), sodium azide (NaN_3, Aldrich), 2-deoxyglucose (2-DG, Aldrich), camptothecin (CPT, 99%, Aldrich), and Taxol (99%, Aldrich). RPMI 1640 cell culture medium, penicillin/streptomycin, L-glutamine, Alexa594 phalloidin, and Hoechst 33342 were purchased from Invitrogen (Carlsbad, CA). Fetal bovine serum (FBS) was from Atlanta Biologicals, Inc. (Lawrenceville, GA). Anti-LAMP-1 and anti-GTP-Rac1 antibody were obtained from Abcam (Cambridge, MA) and Cell Signaling (Danvers, MA). Anti-total-Rac1, anticlathrin, and anticaveolin antibodies were purchased from Santa Cruz Biotechnology (Santa Cruz, CA). Deionized H_2O was obtained from a Millipore water purification system. Toluene (99.5%) refluxed before use.

MSNP Synthesis. MSNPs with different AR were chemically synthesized by a sol−gel approach using a surfactant/co-structure direct agent (CSDA) mixture as template. Different shaped MSNPs and ARs were synthesized by varying the PFOA/CTAB molar ratio as follows: MSNP0 = 0; MSNP1 = 0.015; MSNP2 = 0.03; MSNP3 = 0.06. The PFOA/CTAB mixture was stirred at 600 rpm for 1 h at room temperature before the addition of 2.1 mL of 2 M NaOH. Subsequently, the solution temperature was increased to 80 °C before the addition of 4.1 mL of TEOS. This mixture was stirred for an additional 2 h, and the precipitate was carefully collected by filtration. After washing three times with methanol and deionized water, the solids were air-dried overnight at room temperature. The MSNP templates were removed by extracting the CTAB with HCl containing methanol under nitrogen protection. The resulting MSNPs were collected by filtration, washed by methanol, and dried overnight in air. Depending on the shape and AR, the particles were designated MSNP0, MSNP1, MSNP2, and MSNP3 as explained in Table 1. To visualize the particles under a confocal microscope or perform flow cytometry, FITC- or RITC-labeled MSNPs were prepared by suspending 200 mg of MSNP in 10 mL of dry toluene with 3 μL of APTES, followed by the attachment of FITC or RITC in ethanol. The labeled MSNPs were collected by centrifugation and washed by methanol and water before use.

Physicochemical Characterization of MSNPs. MSNPs were characterized for shape (aspect ratio), surface area, hydrodynamic size, and zeta-potential. The shape and morphology of the MSNPs were characterized by scanning electron microscopy (SEM, JSM-6700F) at 15 kV. The pore structure and aspect ratio were studied by using a transmission electron microscope, JEM 1200-EX operated at 80 kV. Microfilms for TEM imaging were obtained by placing a drop of the respective MSNP suspensions onto a 200-mesh copper TEM grid and drying at room temperature overnight. The AR values were determined by measuring the length and diameter of at least 30 randomly selected particles. X-ray diffraction (XRD) patterns were recorded on a Panalytical X'Pert Pro powder diffractometer with Ni-filtered Cu Kα radiation. UV−vis spectra were collected using a Cary 5000 UV−vis−NIR spectrophotometer. For surface area measurement, N_2 adsorption−desorption isotherms were obtained on a Quadrasorb SI surface area analyzer and pore size analyzer (Quantachrome Instruments, Florida, USA). The BET model was applied to evaluate the specific surface areas, and the Barret−Joyner−Halenda (BJH) method was used to calculate the pore size. Particle hydrodynamic size and zeta-potential were measured in pure water or cell culture medium using a ZetaSizer Nano (Malvern Instruments Ltd., Worcestershire, UK).

MSNP Dispersion and Use To Perform Tissue Culture. All cell cultures were maintained in 75 cm^2 cell culture flasks, in which the cells were passaged at 70−80% confluency every 2−3 days. The human cervical (HeLa) and lung cancer (A549) cells were cultured in RPMI 1640 containing 10% FBS, 100 U/mL penicillin, 100 μg/mL streptomycin, and 2 mM L-glutamine (complete RPMI medium). To disperse MSNP in cell culture medium, the water stock solution was sonicated (Tekmar Sonic Disruptor probe) for 10 s before use. In order to coat the surface of MSNP with FBS, 19 μL of MSNP suspension was mixed with 1 μL of FBS. Complete cell culture medium was then added to the serum-coated MSNP suspension.

Assessment of Cellular MSNP Uptake by Flow Cytometry and Confocal Microscopy. For the performance of flow cytometry, aliquots of 1 $\times$ 10^5 cells (HeLa and A549 cells) were cultured in 12-well plates in 1 mL of complete RPMI medium. RITC-labeled spherical MSNPs were added to the above cultures at 20 μg/mL for 1 h, washed carefully in PBS, and then incubated with different FITC-labeled MSNPs at 20 μg/mL for 6 h in complete RPMI medium. The purpose of prior incubation with the RITC-labeled spheres is to demonstrate that cells can distinguish between a spherical shape and a rod-shaped particle. All cell types were trypsinized and washed in PBS three times. Cells were analyzed in a SCAN flow cytometer using mean FL-2 and FL-1 to assess RITC and FITC fluorescence, respectively. Data are reported as fold increase in mean fluorescence intensity (MFI), using MSNP0 uptake as reference.

For the confocal studies, cellular uptake of the spheres and different AR particles was performed by adding 20 μg/mL FITC-labeled particles to 8-well chamber slides. Each well contained 5 $\times$ 10^4 cells in 0.5 mL of complete culture medium. Cell membranes were costained with 5 μg/mL AlexaFluor633-conjugated wheat germ agglutinin (WGA) in PBS for 30 min. Slides were

mounted with Hoechst 33342 and visualized under a confocal microscope (Leica Confocal 1P/FCS) in the UCLA/CNSI Advanced Light Microscopy/Spectroscopy Shared Facility. High-magnification images were obtained with the 100× objective.

Transmission Electron Microscopy of MSNP-Treated Cells. HeLa cells were treated with each of the MSNP variants at 20 μg/mL for 3 h in complete RPMI. The cells were washed in PBS and immediately fixed with 2.5% glutaraldehyde in PBS. After secondary fixation in 1% OsO_4 in PBS, the cells were dehydrated in a graded ethanol series, treated with propylene oxide, and embedded in resin. Approximately 60−70 nm thick sections were cut on a Leica ultramicrotome and picked up on Formvar-coated copper grids. The sections were examined in a CM120 electron microscope (Philips).

Electron Tomography. TEM grids were used for the tomography imaging on an FEI Tecnai F20 microscope operated at 200 kV. Tilt series were acquired by tilting the specimen from −70 to 70° at 1° increments and with a TIETZ F415MP 16 megapixel CCD camera at a magnification of 26 600× and then aligned using the ETOMO program in the IMOD package.[71] The aligned tilt series were then further processed using the reconstruction Inspect3D program from FEI, with the SIRT option, to improve reconstruction accuracy and contrast. Three-dimensional movies of the aligned tilt series were generated using both Inspect3d and Windows movie maker. Visualization of 3D tomographic reconstructions were performed using 3DMOD of IMOD[71] and Amira (http://www.amira.com/).

F-Actin Staining and Filopodia Counting. HeLa cells were seeded into 8-well chamber slides and incubated with or without MSNP at a concentration of 20 μg/mL in complete RPMI for 6 h. Cells were washed three times in PBS, fixed with 3.7% formaldehyde for 30 min, and permeabilized with 0.25% Triton X-100 for 10 min. For F-actin staining, cells were incubated with Alexa594 phalloidin in the dark for 30 min at room temperature. The slides were viewed using a confocal microscope equipped with a 100× oil-immersion objective. The average number of filopodia per cell as determined by actin fiber staining was calculated by counting at least 20 randomly selected cells in each exposure category.[29] After filopodia counting, two-sided Student's *t* test was performed to determine whether there was a statistically significant difference.[29]

Drug and Temperature Inhibition Studies. HeLa cells were seeded in a 12-well plates at the density of 1×10^5 per well. The cells were precultured in serum-free RPMI 1640 medium containing amiloride (75 μM), Cyto D (2.5 μg/mL), or 0.1% NaN_3/50 mM 2-DG for 3 h. Alternatively, cells were placed at 4 °C. After 3 h pretreatment, the medium was exchanged into fresh complete RPMI 1640 that contained 20 μg/mL FITC-labeled MSNP2, one of the chemical inhibitors (amiloride, Cyto D or NaN_3/2-DG), and 10% FBS for a further 6 h culture time. To observe a temperature effect, the cellular incubation with particles was carried out at 4 °C for 6 h. Following a 6 h incubation period, the cells were washed with PBS and then processed for flow cytometry as described above. The filopodia counting was performed by confocal microscopy as described above. We also conducted experiments with the caveolar and clathrin-coated inhibitors. The cells were precultured in complete RPMI 1640 medium containing filipin (5 μM) or monodansylcadaverine (50 μM) for 3 h. At this time point, the medium was replaced by fresh complete RPMI containing 20 μg/mL FITC-labeled MSNP2 and filipin (5 μM) or monodansylcadaverine (50 μM), and cells were incubated for a further 6 h time period. The cells were washed with PBS and then processed for flow cytometry analysis.

Assessment of Cellular Rac1 Activation. To study Rac1 activation, HeLa cells were serum-starved for 4 h before introduction of the particles that were dispersed in RPMI containing 10% FBS. Cells were incubated with the particles for 30 min at a concentration of 20 μg/mL. Because FBS may also contribute to Rac1 activation due to the presence of growth factors, it was necessary to include a control where serum-starved cells were exposed to complete RPMI for 30 min to allow adjustment for any possible Rac1 activation due to the complete medium. After fixation and permeabilization, cells were stained with antibodies recognizing the activated GTP-bound form of Rac1 or total Rac1 protein.[37−39] The primary antibodies were detected by secondary antibodies conjugated to Alexa594 or FITC, respectively. Nuclei were stained by Hoechst 33342. The Alexa594 fluorescence intensity as a measure of Rac1 activation was determined by ImageJ software. The fluorescence intensity of control cells incubated in serum-containing medium for 30 min was chosen as reference with fluorescent intensity = 1. The fluorescence intensity of cells treated with the various MSNPs was then expressed as the fold increase compared to this control value. The experiment was repeated in presence of amiloride, Cyto D, NaN_3/2-DG, as well as at 4 °C as described above.

In order to further confirm the confocal data, particle-induced Rac1 activation was detected by a pull-down assay using configuration-specific monoclonal antibody Rac activation assay kit (NewEast Biosciences, PA) according to the manufacture's instruction. Briefly, HeLa cells were seeded into 10 cm tissue culture dish ($\sim 2 \times 10^7$ cells/dish) and received the various particle treatments as described above. After cold PBS washing three times, 1 mL of ice-cold lysis buffer was added to the cells. Aliquots of each cell lysate were added to two microcentrifuge tubes, one for analysis of the active and the other for the analysis of total Rac1 content. The protein content of the supernatants was determined by the Bradford method. After the addition of 1 μL of the monoclonal antibody recognizing active Rac1, the cell lysates received the addition of 20 μL of protein A/G agarose beads. After incubation at 4 °C for 1 h with gentle agitation, the beads were collected and washed by lysis buffer three times. Following the resuspension of the bead pellet in 20 μL of SDS-PAGE sample buffer, the samples were electrophoresed by 12% SDS-PAGE and transferred to a PVDF membrane. After blocking, the membranes were incubated with 1:1000 dilution of primary polyclonal antibody to Rac1 (Santa Cruz Biotechnology, CA). The membranes were overlaid with goat anti-mouse secondary antibody (1:1000 dilution) before the addition of the HRP-conjugated streptavidin−biotin complex. The proteins were detected by using the ECL reagent according to the manufacturer's instructions. The total Rac1 protein was detected by Western blotting using anti-Rac1 antibody (Santa Cruz Biotechnology, CA).

Drug Loading and Loading Capacity Measurement. Two hydrophobic anticancer drugs, Taxol and camptothecin (CPT), were loaded into different MSNPs using 20 mg of each type of particles suspended into a solution containing 0.5 mg of each drug in 1 mL of DMSO. After 24 h, the particles were collected by centrifugation, and the trace amounts of DMSO were removed by drying under vacuum. The drug-laden particles were washed and stored as an aqueous stock solution at 20 mg/mL. To measure the loading capacity of the particles, they were resuspended in methanol and thoroughly sonicated to remove the drug from the pores. After centrifugation and removal of the supernatant, the process was repeated three times to elute all drug. The supernatants were combined, and the amount of free drug was calculated using Taxol absorbance at 229 nm and the CPT fluorescence at excitation and emission wavelengths of 370 and 448 nm, respectively, in a microplate reader (SpectraMax M5Microplate Reader, Molecular Device, USA).

Assessment of HeLa Cytotoxicity in Response to Treatment with Drug-Loaded Particles. HeLa cells were plated at 1×10^4 cells per well in 96-well plates. MSNPs, loaded with CPT or Taxol, were incubated with the cells to deliver CPT concentrations of 0.1−8.0 μg/mL and Taxol concentrations of 0.1−2.0 μg/mL for 36 h. The effect of the MSNP-bound drug was compared to similar amounts of free drug delivered in DMSO/PBS. A MTS assay was performed 36 h after drug and particle exposure to assess cellular viability as previous described.[13]

Statistical Analysis. Data represent the mean ± SD for duplicate or triplicate measurements in each experiment. Differences between the mean values were analyzed by two-sided Student's *t* test or one way ANOVA. All experiments were repeated at least twice.

Acknowledgment. This study was funded by the U.S. Public Health Service Grants, U19 ES019528 (UCLA Center for Nano-Biology and Predictive Toxicology) as well as RO1 CA133697, RO1 ES016746, and RC2 ES018766. Support for this study was

also provided the National Science Foundation and the Environmental Protection Agency under Cooperative Agreement Number DBI-0830117. The work was also supported by the NSF USDOD HDTRA 1-08-1-0041 grants and Grant 53292 from the Bill & Melinda Gates Foundation through the Grand Challenges Exploration Initiative. We acknowledge the use of electron microscope facilities in the UCLA Electron Imaging Center for NanoMachines supported by NIH (1S10RR23057 to Z.H.Z.).

Supporting Information Available: Additional figures, results, and method descriptions as described in the text. This material is available free of charge *via* the Internet at http://pubs.acs.org.

REFERENCES AND NOTES

1. Gratton, S. E. A.; Ropp, P. A.; Pohlhaus, P. D.; Luft, J. C.; Madden, V. J.; Napier, M. E.; DeSimone, J. M. The Effect of Particle Design on Cellular Internalization Pathways. *Proc. Natl. Acad. Sci. U.S.A.* **2008**, *105*, 11613–11618.
2. Decuzzi, P.; Godin, B.; Tanaka, T.; Lee, S. Y.; Chiappini, C.; Liu, X.; Ferrari, M. Size and Shape Effects in the Biodistribution of Intravascularly Injected Particles. *J. Controlled Release* **2010**, *141*, 320–327.
3. Mitragotri, S.; Lahann, J. Physical Approaches to Biomaterial Design. *Nat. Mater.* **2009**, *8*, 15–23.
4. Chithrani, B. D.; Ghazani, A. A.; Chan, W. C. W. Determining the Size and Shape Dependence of Gold Nanoparticle Uptake into Mammalian Cells. *Nano Lett.* **2006**, *6*, 662–668.
5. Yang, S.; Zhou, X.; Yuan, P.; Yu, M.; Xie, S.; Zou, J.; Lu, G.; Yu, C. Siliceous Nanopods from a Compromised Dual-Templating Approach. *Angew. Chem., Int. Ed.* **2007**, *46*, 8579–8582.
6. Doshi, N.; Mitragotri, S. Macrophages Recognize Size and Shape of Their Targets. *PLoS ONE* **2010**, *5*, e10051.
7. Lee, S.-Y.; Ferrari, M.; Decuzzi, P. Shaping Nano-/Microparticles for Enhanced Vascular Interaction in Laminar Flows. *Nanotechnology* **2009**, *20*, 495101.
8. Champion, J. A.; Katare, Y. K.; Mitragotri, S. Particle Shape: A New Design Parameter for Micro- and Nanoscale Drug Delivery Carriers. *J. Controlled Release* **2007**, *121*, 3–9.
9. Meng, H.; Xia, T.; George, S.; Nel, A. E. A Predictive Toxicological Paradigm for the Safety Assessment of Nanomaterials. *ACS Nano* **2009**, *3*, 1620–1627.
10. Nel, A. E.; Madler, L.; Velegol, D.; Xia, T.; Hoek, E. M. V.; Somasundaran, P.; Klaessig, F.; Castranova, V.; Thompson, M. Understanding Biophysicochemical Interactions at the Nano-Bio Interface. *Nat. Mater.* **2009**, *8*, 543–557.
11. Lu, J.; Liong, M.; Zink, J. I.; Tamanoi, F. Mesoporous Silica Nanoparticles as a Delivery System for Hydrophobic Anticancer Drugs. *Small* **2007**, *3*, 1341–1346.
12. Meng, H.; Liong, M.; Xia, T.; Li, Z.; Ji, Z.; Zink, J. I.; Nel, A. E. Engineered Design of Mesoporous Silica Nanoparticles to Deliver Doxorubicin and P-Glycoprotein siRNA To Overcome Drug Resistance in a Cancer Cell Line. *ACS Nano* **2010**, *4*, 4539–4550.
13. Xia, T.; Kovochich, M.; Liong, M.; Meng, H.; Kabehie, S.; George, S.; Zink, J. I.; Nel, A. E. Polyethyleneimine Coating Enhances the Cellular Uptake of Mesoporous Silica Nanoparticles and Allows Safe Delivery of siRNA and DNA Constructs. *ACS Nano* **2009**, *3*, 3273–3286.
14. Liong, M.; Lu, J.; Kovochich, M.; Xia, T.; Ruehm, S. G.; Nel, A. E.; Tamanoi, F.; Zink, J. I. Multifunctional Inorganic Nanoparticles for Imaging, Targeting, and Drug Delivery. *ACS Nano* **2008**, *2*, 889–896.
15. Meng, H.; Xue, M.; Xia, T.; Zhao, Y.-L.; Tamanoi, F.; Stoddart, J. F.; Zink, J. I.; Nel, A. E. Autonomous *In Vitro* Anticancer Drug Release from Mesoporous Silica Nanoparticles by pH-Sensitive Nanovalves. *J. Am. Chem. Soc.* **2010**, *132*, 12690–12697.
16. Liong, M.; Angelos, S.; Choi, E.; Patel, K.; Stoddart, J. F.; Zink, J. I. Mesostructured Multifunctional Nanoparticles for Imaging and Drug Delivery. *J. Mater. Chem.* **2009**, *19*, 6251–6257.
17. Ferris, D. P.; Zhao, Y.-L.; Khashab, N. M.; Khatib, H. A.; Stoddart, J. F.; Zink, J. I. Light-Operated Mechanized Nanoparticles. *J. Am. Chem. Soc.* **2009**, *131*, 1686–1688.
18. Coti, K. K.; Belowich, M. E.; Liong, M.; Ambrogio, M. W.; Lau, Y. A.; Khatib, H. A.; Zink, J. I.; Khashab, N. M.; Stoddart, J. F. Mechanised Nanoparticles for Drug Delivery. *Nanoscale* **2009**, *1*, 16–39.
19. Yang, S.; Zhao, L.; Yu, C.; Zhou, X.; Tang, J.; Yuan, P.; Chen, D.; Zhao, D. On the Origin of Helical Mesostructures. *J. Am. Chem. Soc.* **2006**, *128*, 10460–10466.
20. Kresge, C. T.; Leonowicz, M. E.; Roth, W. J.; Vartuli, J. C.; Beck, J. S. Ordered Mesoporous Molecular Sieves Synthesized by a Liquid-Crystal Template Mechanism. *Nature* **1992**, *359*, 710–712.
21. Zhang, L.; Qiao, S. Z.; Cheng, L.; Yan, Z.; Lu, G. Q. M. Fabrication of a Magnetic Helical Mesostructured Silica Rod. *Nanotechnology* **2008**, *19*, 435608.
22. Ohsuna, T.; Liu, Z.; Che, S.; Terasaki, O. Characterization of Chiral Mesoporous Materials by Transmission Electron Microscopy. *Small* **2005**, *1*, 233–237.
23. Huang, X.; Teng, X.; Chen, D.; Tang, F.; He, J. The Effect of the Shape of Mesoporous Silica Nanoparticles on Cellular Uptake and Cell Function. *Biomaterials* **2010**, *31*, 438–448.
24. Dausend, J.; Musyanovych, A.; Dass, M.; Walther, P.; Schrezenmeier, H.; Landfester, K.; Mailänder, V. Uptake Mechanism of Oppositely Charged Fluorescent Nanoparticles in HeLa Cells. *Macromol. Biosci.* **2008**, *8*, 1135–1143.
25. Kalin, S.; Amstutz, B.; Gastaldelli, M.; Wolfrum, N.; Boucke, K.; Havenga, M.; DiGennaro, F.; Liska, N.; Hemmi, S.; Greber, U. F. Macropinocytotic Uptake and Infection of Human Epithelial Cells with Species B2 Adenovirus Type 35. *J. Virol.* **2010**, *84*, 5336–5350.
26. Mercer, J.; Helenius, A. Virus Entry by Macropinocytosis. *Nat. Cell Biol.* **2009**, *11*, 510–520.
27. Nakase, I.; Niwa, M.; Takeuchi, T.; Sonomura, K.; Kawabata, N.; Koike, Y.; Takehashi, M.; Tanaka, S.; Ueda, K.; Simpson, J. C.; *et al.* Cellular Uptake of Arginine-Rich Peptides: Roles for Macropinocytosis and Actin Rearrangement. *Mol. Ther.* **2004**, *10*, 1011–1022.
28. Hillaireau, H.; Couvreur, P. Nanocarriers' Entry into the Cell: Relevance to Drug Delivery. *Cell. Mol. Life Sci.* **2009**, *66*, 2873–2896.
29. Sheldon, H.; Andre, M.; Legg, J. A.; Heal, P.; Herbert, J. M.; Sainson, R.; Sharma, A. S.; Kitajewski, J. K.; Heath, V. L.; Bicknell, R. Active Involvement of Robo1 and Robo4 in Filopodia Formation and Endothelial Cell Motility Mediated *via* WASP and Other Actin Nucleation-Promoting Factors. *FASEB J.* **2009**, *23*, 513–522.
30. West, M. A.; Bretscher, M. S.; C, W. Distinct Endocytotic Pathways in Epidermal Growth Factor-Stimulated Human Carcinoma A431 Cells. *J. Cell Biol.* **1989**, *109*, 2731–2739.
31. Schrijvers, D. M.; Martinet, W.; De Meyer, G. R. Y.; Andries, L.; Herman, A. G.; Kockx, M. M. Flow Cytometric Evaluation of a Model for Phagocytosis of Cells Undergoing Apoptosis. *J. Immunol. Methods* **2004**, *287*, 101–108.
32. Greyner, H. J.; Wiraszka, T.; Zhang, L.-S.; Petroll, W. M.; Mummert, M. E. Inducible Macropinocytosis of Hyaluronan in B16-F10 Melanoma Cells. *Matrix Biol.* **2010**, *29*, 503–510.
33. von Delwig, A.; Hilkens, C.; Altmann, D.; Holmdahl, R.; Isaacs, J.; Harding, C.; Robertson, H.; McKie, N.; Robinson, J. Inhibition of Macropinocytosis Blocks Antigen Presentation of Type II Collagen *In Vitro* and *In Vivo* In HLA-DR1 Transgenic Mice. *Arthritis Res. Ther.* **2006**, *8*, 1–11.
34. Li, W.; Chen, C.; Ye, C.; Wei, T.; Zhao, Y. Z.; Lao, F. L.; Chen, Z.; Meng, H.; Gao, Y.; Yuan, H.; *et al.* The Translocation of Fullerenic Nanoparticles into Lysosome *via* the Pathway of Clathrin-Mediated Endocytosis. *Nanotechnology* **2008**, *19*, 145102.
35. Conner, S. D.; Schmid, S. L. Regulated Portals of Entry into the Cell. *Nature* **2003**, *422*, 37–44.
36. Ridley, A. J.; Paterson, H. F.; Johnston, C. L.; Diekmann, D.; Hall, A. The Small GTP-Binding Protein Rac Regulates Growth Factor-Induced Membrane Ruffling. *Cell* **1992**, *70*, 401–410.

37. Li, Q.; Ho, C. S.; Marinescu, V.; Bhatti, H.; Bokoch, G. M.; Ernst, S. A.; Holz, R. W.; Stuenkel, E. L. Facilitation of Ca^{2+}-Dependent Exocytosis by Rac1-GTPase in Bovine Chromaffin Cells. *J. Physiol.* **2003**, *550*, 431–445.
38. Osada, T.; Watanabe, S.; Tanaka, H.; Hirose, M.; Miyazaki, A.; Sato, N. Effect of Mechanical Strain on Gastric Cellular Migration and Proliferation During Mucosal Healing: Role of Rho Dependent and Rac Dependent Cytoskeletal Reorganisation. *Gut* **1999**, *45*, 508–515.
39. Ueda, S.; Kataoka, T.; Satoh, T. Activation of the Small GTPase Rac1 by a Specific Guanine-Nucleotide-Exchange Factor Suffices To Induce Glucose Uptake into Skeletal-Muscle Cells. *Biol. Cell* **2008**, *100*, 645–657.
40. Clements, B. A.; Incani, V.; Kucharski, C.; Lavasanifar, A.; Ritchie, B.; Uludag, H. A Comparative Evaluation of Poly-L-lysine-palmitic Acid and Lipofectamine (TM) 2000 for Plasmid Delivery to Bone Marrow Stromal Cells. *Biomaterials* **2007**, *28*, 4693–4704.
41. Jackson, A. L.; Linsley, P. S. Recognizing and Avoiding siRna Off-Target Effects for Target Identification and Therapeutic Application. *Nat. Rev. Drug Discovery* **2010**, *9*, 57–67.
42. Koivusalo, M.; Welch, C.; Hayashi, H.; Scott, C. C.; Kim, M.; Alexander, T.; Touret, N.; Hahn, K. M.; Grinstein, S. Amiloride Inhibits Macropinocytosis by Lowering Submembranous pH and Preventing Rac1 and Cdc42 Signaling. *J. Cell Biol.* **2010**, *188*, 547–563.
43. Mercer, J.; Knebel, S.; Schmidt, F. I.; Crouse, J.; Burkard, C.; Helenius, A. Vaccinia Virus Strains Use Distinct Forms of Macropinocytosis for Host−Cell Entry. *Proc. Natl. Acad. Sci. U.S.A.* **2010**, *107*, 9346–9351.
44. Slowing, I. I.; Trewyn, B. G.; Lin, V. S. Y. Mesoporous Silica Nanoparticles for Intracellular Delivery of Membrane-Impermeable Proteins. *J. Am. Chem. Soc.* **2007**, *129*, 8845–8849.
45. Champion, J. A.; Mitragotri, S. Role of Target Geometry in Phagocytosis. *Proc. Natl. Acad. Sci. U.S.A.* **2006**, *103*, 4930–4934.
46. Simone, E. A.; Dziubla, T. D.; Muzykantov, V. R. Polymeric Carriers: Role of Geometry in Drug Delivery. *Expert Opin. Drug Delivery* **2008**, *5*, 1283–1300.
47. Decuzzi, P.; Ferrari, M. The Receptor-Mediated Endocytosis of Nonspherical Particles. *Biophys. J.* **2008**, *94*, 3790–3797.
48. Champion, J. A.; Katare, Y. K.; Mitragotri, S. Making Polymeric Micro- and Nanoparticles of Complex Shapes. *Proc. Natl. Acad. Sci. U.S.A.* **2007**, *104*, 11901–11904.
49. Arnida; Malugin, A.; Ghandehari, H. Cellular Uptake and Toxicity of Gold Nanoparticles in Prostate Cancer Cells: A Comparative Study of Rods and Spheres. *J. Appl. Toxicol.* **2010**, *30*, 212–217.
50. Chithrani, B. D.; Chan, W. C. W. Elucidating the Mechanism of Cellular Uptake and Removal of Protein-Coated Gold Nanoparticles of Different Sizes and Shapes. *Nano Lett.* **2007**, *7*, 1542–1550.
51. Muro, S.; Garnacho, C.; Champion, J. A.; Leferovich, J.; Gajewski, C.; Schuchman, E. H.; Mitragotri, S.; Muzykantov, V. R. Control of Endothelial Targeting and Intracellular Delivery of Therapeutic Enzymes by Modulating the Size and Shape of ICAM-1-Targeted Carriers. *Mol. Ther.* **2008**, *16*, 1450–1458.
52. Hayakawa, K.; Tatsumi, H.; Sokabe, M. Actin Stress Fibers Transmit and Focus Force To Activate Mechanosensitive Channels. *J. Cell Sci.* **2008**, *121*, 496–503.
53. Fiorentini, C.; Falzano, L.; Fabbri, A.; Stringaro, A.; Logozzi, M.; Travaglione, S.; Contamin, S.; Arancia, G.; Malorni, W.; Fais, S. Activation of Rho GTPases by Cytotoxic Necrotizing Factor 1 Induces Macropinocytosis and Scavenging Activity in Epithelial Cells. *Mol. Biol. Cell* **2001**, *12*, 2061–2073.
54. Muro, S.; Wiewrodt, R.; Thomas, A.; Koniaris, L.; Albelda, S. M.; Muzykantov, V. R.; Koval, M. A Novel Endocytic Pathway Induced by Clustering Endothelial ICAM-1 or PECAM-1. *J. Cell. Sci.* **2003**, *116*, 1599–1609.
55. Dharmawardhane, S.; Schurmann, A.; Sells, M. A.; Chernoff, J.; Schmid, S. L.; Bokoch, G. M. Regulation of Macropinocytosis by p21-Activated Kinase-1. *Mol. Biol. Cell* **2000**, *11*, 3341–3352.
56. Chen, L.-M.; Hobbie, S.; Galan, J. E. Requirement of CDC42 for Salmonella-Induced Cytoskeletal and Nuclear Responses. *Science* **1996**, *274*, 2115–2118.
57. Sandgren, K. J.; Wilkinson, J.; Miranda-Saksena, M.; McInerney, G. M.; Byth-Wilson, K.; Robinson, P. J.; Cunningham, A. L. A Differential Role for Macropinocytosis in Mediating Entry of the Two Forms of Vaccinia Virus into Dendritic Cells. *PLoS Pathog.* **2010**, *6*, e1000866.
58. Sahay, G.; Alakhova, D. Y.; Kabanov, A. V. Endocytosis of Nanomedicines. *J. Controlled Release* **2010**, *145*, 182–195.
59. Geiger, B.; Spatz, J. P.; Bershadsky, A. D. Environmental Sensing through Focal Adhesions. *Nat. Rev. Mol. Cell Biol.* **2009**, *10*, 21–33.
60. Discher, D. E.; Janmey, P.; Wang, Y. Tissue Cells Feel and Respond to the Stiffness of Their Substrate. *Science* **2005**, *310*, 1139–1143.
61. Thery, M.; Racine, V.; Piel, M.; Pepin, A.; Dimitrov, A.; Chen, Y.; Sibarita, J.-B.; Bornens, M. Anisotropy of Cell Adhesive Microenvironment Governs Cell Internal Organization and Orientation of Polarity. *Proc. Natl. Acad. Sci. U.S.A.* **2006**, *103*, 19771–19776.
62. Butler, B.; Gao, C.; Mersich, A. T.; Blystone, S. D. Purified Integrin Adhesion Complexes Exhibit Actin-Polymerization Activity. *Curr. Biol.* **2006**, *16*, 242–251.
63. Roiter, Y.; Ornatska, M.; Rammohan, A. R.; Balakrishnan, J.; Heine, D. R.; Minko, S. Interaction of Nanoparticles with Lipid Membrane. *Nano Lett.* **2008**, *8*, 941–944.
64. Slowing, I. I.; Wu, C. W.; Vivero-Escoto, J. L.; Lin, V. S. Y. Mesoporous Silica Nanoparticles for Reducing Hemolytic Activity Towards Mammalian Red Blood Cells. *Small* **2009**, *5*, 57–62.
65. Glass, R.; Arnold, M.; Blümmel, J.; Küller, A.; Möller, M.; Spatz, J. P. Micro-nanostructured Interfaces Fabricated by the Use of Inorganic Block Copolymer Micellar Monolayers as Negative Resist for Electron-Beam Lithography. *Adv. Funct. Mater.* **2003**, *13*, 569–575.
66. Glass, R.; Arnold, M.; Cavalcanti-Adam, E. A.; Blümmel, J.; Haferkemper, C.; Dodd, C.; Spatz, J. P. Block Copolymer Micelle Nanolithography on Non-conductive Substrates. *New J. Phys.* **2004**, *6*, 101.
67. Arnold, M.; Cavalcanti-Adam, E. A.; Glass, R.; Blümmel, J.; Eck, W.; Kantlehner, M.; Kessler, H.; Spatz, J. P. Activation of Integrin Function by Nanopatterned Adhesive Interfaces. *ChemPhysChem* **2004**, *5*, 383–388.
68. Cavalcanti-Adam, E. A.; Volberg, T.; Micoulet, A.; Kessler, H.; Geiger, B.; Spatz, J. P. Cell Spreading and Focal Adhesion Dynamics Are Regulated by Spacing of Integrin Ligands. *Biophys. J.* **2007**, *92*, 2964–2974.
69. Karmali, P. P.; Kotamraju, V. R.; Kastantin, M.; Black, M.; Missirlis, D.; Tirrell, M.; Ruoslahti, E. Targeting of Albumin-Embedded Paclitaxel Nanoparticles to Tumors. *Nanomedicine* **2009**, *5*, 73–82.
70. Lobo, C.; Lopes, G.; Silva, O.; Gluck, S. Paclitaxel Albumin-Bound Particles (Abraxane(TM)) in Combination with Bevacizumab with or without Gemcitabine: Early Experience at the University of Miami/Braman Family Breast Cancer Institute. *Biomed. Pharmacother.* **2007**, *61*, 531–533.
71. Kremer, J. R.; Mastronarde, D. N.; McIntosh, J. R. Computer Visualization of Three-Dimensional Image Data Using IMOD. *J. Struct. Biol.* **1996**, *116*, 71–76.